Master's Thesis

Residence and diffusion of a dynamically prototropic hydration probe in AOT reverse micelles

Jae-Heon Park

Department of Chemistry

Ulsan National Institute of Science and Technology

2021

Residence and diffusion of a dynamically prototropic hydration probe in AOT reverse micelles

Jae-Heon Park

Department of Chemistry

Ulsan National Institute of Science and Technology

Residence and diffusion of a dynamically prototropic hydration probe in AOT reverse micelles

A thesis submitted to UNIST
in partial fulfillment of the
requirements for the degree of
Master of Science

Jae-Heon Park

12.10.2020
Approved by

_____

Advisor
Associate professor Oh-Hoon Kwon

Residence and diffusion of a dynamically prototropic hydration probe in AOT reverse micelles

Jae-Heon Park

This certifies that the thesis of Jae-Heon Park is approved.

12.10.2020

Signature

_____

Advisor: Associate professor Oh-Hoon Kwon

Signature

_____

Associate professor Yung Sam Kim

Signature

_____

Associate professor Bum Suk Zhao

Abstract

We investigated the hydration dynamics in the nanosized water pool of an Aerosol-OT (AOT) reverse micelle (RM) using a prototropic (proton-donating) fluorescent dye, *N*-methyl-7-hydroxyquinolinium ($NM7HQ^+$), as the probe. $NM7HQ^+$ is a photoacid, and the deprotonation of its excited-state cationic form (C*) gives rise to a neutral keto species (K*). In the present study, the residence sites of C* and K* in water pools of various sizes were determined by monitoring their time-resolved fluorescence anisotropy. Additionally, the evolutions of the C* and K* bands in the time-resolved fluorescence spectra were analyzed by fitting the spectra to the sum of two lognormal peak functions. The time-dependent spectral shifts of the species with different formal charges revealed the characteristic hydration behavior at the interface of the anionic AOT headgroups and the bound water region, as well as the rotational and translational diffusion of the probe within the RM.

This thesis was adapted from the publication A. Adhikari, J.-H. Park, H.-W. Nho and O.-H. Kwon, *J. Mol. Liq.*, **2020**, *320*, 114346.

Contents

List of Figures & Scheme

Figure 7. Deconvolution of the TRES of $NM7HQ^+$ in water/AOT/*n*-heptane RMs at $w_0 = 8$. The long- and short-dashed lines represent the deconvoluted spectra of C* and K*, respectively.

Figure 8. $\nu(t)$ profiles of $NM7HQ^+$ in the water/AOT/*n*-heptane RMs: (a) C* bands and (b) K* bands with $\lambda_{ex} = 375$ nm, and (c) K* bands with $\lambda_{ex} = 450$ nm for different w_0 values.

Figure 9. $\nu(t)$ profiles of $NM7HQ^+$ in water/AOT/*n*-heptane RMs for the K* bands at $\lambda_{ex} = 375$ nm (red line) and $\lambda_{ex} = 450$ nm (blue line) at different w_0 values.

Figure 10. Fluorescence anisotropy decay profiles with $\lambda_{ex} = 375$ nm monitored at (a) 450 nm and (b) 550 nm, and (c) the profiles with $\lambda_{ex} = 450$ nm monitored at 550 nm of $NM7HQ^+$ in the water/AOT/*n*-heptane RMs at different w_0 values.

Figure 11. Schematic depicting the rotational motion and hydration of $NM7HQ^+$ following ESPT-assisted diffusion within the water/AOT/*n*-heptane RM for the (a) C*- and (b) K*-form probes.

List of Table

I. Introduction

Studies of the hydration dynamics in reverse micelles (RMs) can provide insights into physicochemical phenomena in various confined systems [1–5]. For example, the water pools formed in RMs mimic the water confined in the cavities of organized assemblies or bound water at the surfaces of proteins. In general, RM systems consist of three distinct phases: a continuous outer non-polar solvent phase, an amphiphilic surfactant layer, and a confined inner polar solvent phase (**Figure 1**). Aerosol-OT (AOT, sodium bis(2-ethylhexyl)-sulfosuccinate) is one of the most widely used amphiphilic surfactants for forming RMs. Its molecular structure consists of two long hydrocarbon chains and an anionic sulfonate headgroup. In the formation of AOT RMs, the tails are directed toward the outer non-polar phase, while the charged headgroups aggregate to enclose a nanosized water pool within the RM. The hydration dynamics in the water pool can be studied by following the time-dependent Stokes shift of a fluorescent probe [6–8]. Many reports have indicated that the hydration dynamics in the inner water pool are distinct from those of bulk-phase water [6].

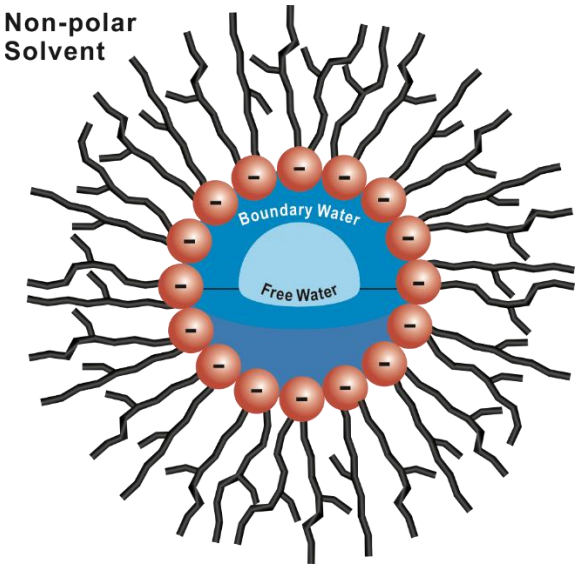

Figure 1. Schematic diagram of an AOT RM. The outer region is occupied by a non-polar solvent. The water pool is divided into two regions: Bound water (deep blue) and free water (light blue). The non-polar solvent and the water pool are separated by a single layer of AOT.

The water pool is often regarded as being spatially segregated into two regions characterized by different kinds of water: the “bound” water near the headgroups and the “free” water located at the core of the water pool [6,9–11]. The bound water molecules experience strong dipole–ion interactions that retard their motion and cause slow hydration. The dynamic properties of the free water are similar to those of bulk water, as the core of the RM is outside the effective range of the AOT headgroups [12–14]. The size of the water pool is described by the parameter w_0, which represents the ratio of the concentration of water to that of AOT:

$$w_0 = [H_2O]/[AOT] \quad (1)$$

Molecules and ions in biological systems often experience changes in the charge state during reactions. In RMs, the charge state of a hydration probe dictates its location along the radial electrostatic gradient from the ionic headgroup sphere to the core of the water pool [15–22]. In the present study, we introduce a unique fluorescent prototropic (proton-donating) probe, *N*-methyl-7-hydroxyquinolinium ($NM7HQ^+$) iodide, to investigate the local hydration dynamics within the AOT RM system, with an emphasis on the changes in its diffusion dynamics in response to the change in its charge state following photoinduced deprotonation. In the ground state, two prototropic forms of $NM7HQ^+$ are in equilibrium, namely, the major protonated cationic form (C) and the minor deprotonated zwitterionic form (Z). Upon photoexcitation, the acidity of $NM7HQ^+$ increases drastically; its pK_a value decreases from 5.9 in the ground state to −2.3 in the excited state [23–26]. Thus, in the excited state, the equilibrium shifts toward the keto form (K*) resulting from the deprotonation of C* (**Scheme 1**). The positive C* is transformed into the neutral K* via excited-state proton transfer (ESPT) to water. In this regard, our prototype probe is unique. The positively charged C form is expected to be localized in the vicinity of the interfacial region between the headgroups and the water pool because of its strong ion–ion interaction with the anionic headgroups. In contrast, the deprotonated Z form, which is in equilibrium with C in the ground state, is anticipated to reside farther from the charged interface because of its neutral formal charge. Upon photoexcitation, C undergoes ESPT to yield the deprotonated, neutral K* form, wherein the strong ion–ion interactions between the probe and the anionic headgroups are replaced with weaker dipole–ion interactions. The dynamic charge state of $NM7HQ^+$ thus offers a unique opportunity to explore local hydration and diffusion behavior, along with the ESPT.

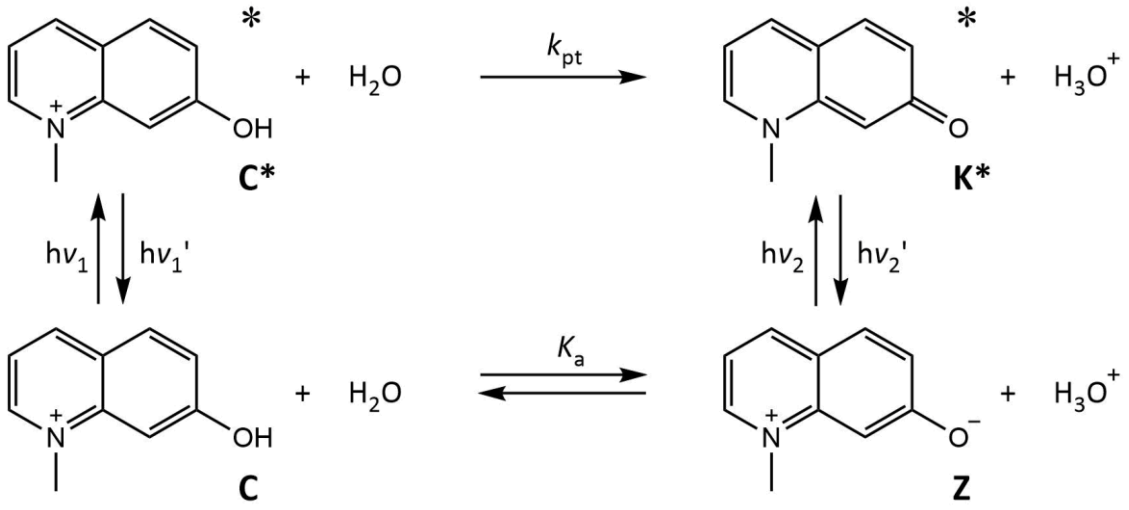

Scheme 1. Photocycle depicting a simplified kinetic scheme of the proton transfer of $NM7HQ^+$. K_a and k_{pt} denote the equilibrium constant in the ground state and the forward rate constant of ESPT, respectively.

In this work, we determined the location of the hydration probe having two different charge states by examining its fluorescence anisotropy decay. In addition, by separating the spectral relaxation of each of the prototropic species in the time-resolved fluorescence spectra, we revealed the unique hydration and diffusion characteristics of the probe resulting from ESPT within the water pool, which should provide insight into chemical processes in biologically relevant environments.

II. Material and methods

2.1. Materials

$NM7HQ^+$ iodide was prepared by refluxing 7-hydroxyquinoline (>99%, Acros Organics) with methyl iodide (>99%, Sigma-Aldrich) in dried toluene for 2 days. The solid product was precipitated by adding diethyl ether to the solution, separated, and recrystallized in an ethanol–ether mixture. $NM7HQ^+$ iodide was dissolved in a 0.1 M AOT (sodium bis(2-ethylhexyl)-sulfosuccinate, BioXtra, >99%, Sigma-Aldrich) solution in *n*-heptane (anhydrous, >99%, Sigma-Aldrich) to provide an $NM7HQ^+$ concentration of 1.0×10^{-4} M. Because AOT is hygroscopic, the initial amount of water in 0.1MAOT in *n*-heptane was determined using Karl Fischer titration, and the initial "dry" w_0 value was calculated to be approximately 0.5. To form water pools in the solution, deionized water (18.2 MΩ·cm, Milli-Q Integral ultrapure water, Millipore Corp.) was added to a 1 cm quartz cuvette containing 2 mL of the solution to achieve the desired w_0 value. The concentration of $NM7HQ^+$ was kept at 1.0×10^{-4} M for all the tertiary mixtures.

2.2. Steady-state and time-resolved spectral measurements

UV/vis absorption and fluorescence spectra were measured using a UV/vis spectrophotometer (V-730, Jasco) and a fluorometer (QM-400, Photon Technology International), respectively. To obtain the TRES and anisotropy values, a time correlated single-photon counting (TCSPC) spectrofluorometer (Fluotime 300, PicoQuant) was used, with picosecond laser diode heads emitting at 375 nm (LDH-D-C-375, PicoQuant) and 450 nm (LDH-D-C-450, PicoQuant) as excitation sources. Fluorescence kinetic profiles were collected at 5 nm intervals from 400 nm to 600 nm, and the collected profiles were transposed to construct the TRES as a function of time. The wavelength-dependent sensitivities of the steady-state and time-resolved spectrometers were calibrated.

For time-resolved fluorescence anisotropy measurements, the polarization of the excitation source was kept fixed in the vertical direction, and the fluorescence kinetic profiles were obtained serially both parallel and perpendicular to the excitation polarization. The time-dependent anisotropy, r(t), was obtained as $r(t) = [I_{VV}(t) - G \cdot I_{VH}(t)]/[I_{VV}(t) + 2G \cdot I_{VH}(_t)]$, where $I_{VV}(t)$, $I_{VH}(t)$, and G denote the fluorescence kinetic profiles obtained parallel and perpendicular to the excitation polarization and the *G*-factor, respectively. The *G*-factor was estimated using the tail matching method to compensate for the polarization-dependent detection efficiency at long timescales. The instrument response function (IRF) was determined to be approximately 150 ps. All measurements were performed at room temperature (295 K).

2.3. Data analysis

The TRES, which depict the time evolution of the emission intensity, $I(t)$, and the peak position, $\nu(t)$, for each of the constituent fluorescence bands, were fit to the sum of lognormal peak functions [27–31]. The spectral shape function, $S(\nu, t)$was expressed as follows:

$$S(\nu, t) = \sum_{n=1}^{2} I_n(t) \cdot \exp\left[(-\ln 2)\times\left\{\frac{\ln\left(1+2b_n\frac{\nu_n(t)-\nu_n(\infty)}{w_n}\right)}{b_n}\right\}^2\right], \quad (2)$$

where $\nu_n(t)$ and $\nu_n(\infty)$ are the wavenumbers at time t and at infinity (i.e., the wavenumber when all relevant excited-state phenomena are over), respectively. b_n and w_n are the asymmetric factor and the spectral width of the n-th peak, respectively. Among these parameters, we focused on the $\nu(t)$ profiles, which reveal the hydration dynamics and diffusion of each prototropic species involved in the ESPT accompanying the positive-to-neutral charge evolution of $NM7HQ^+$. The extracted $\nu_n(t)$ profiles were fit to multi-exponential decay functions as follows:

$$\nu(t) = \nu_\infty + \sum_{i=1}^{k} \nu_i \cdot \exp\left(-\frac{t}{\tau_i}\right) \quad (3)$$

where ν_i is the spectral shift in wavenumber and τ_i is the correlation time of the i-th component.

2.4. DFT calculations

To quantify the dipole moments of the ground state forms of $NM7HQ^+$ (C and Z), DFT calculations were performed using the CAMB3LYP functional with the 6-311G+(d, p) basis sets. For the geometry optimizations of C* and K*, time-dependent density-functional theory (TDDFT) calculations were implemented. The solvent effects of water in the S_0 and S_1 were included via the polarizable continuum model (PCM) using the integral equation formalism variant (IEFPCM) for all the calculations. All calculations were performed using Gaussian 09 (Gaussian, Inc.) software.

III. Results

3.1. Steady-state absorption and emission spectra

The area-normalized absorption spectra presented in **Figure 2(a)** show the equilibrium between the two prototropic species in the ground state: The maximum of the C band was located at approximately 375 nm, while the Z band was observed at >400nm. The emission spectra were obtained by the excitation of C at 375 nm (**Figure 2(b)**) and Z at 450 nm (**Figure 2(c)**). The fluorescence band of C* was observed at around 430 nm when $w_0 = 0.5$. The formation of K* from C* via ESPT was more pronounced at larger w_0 values, and the K* band was located at approximately 520 nm.

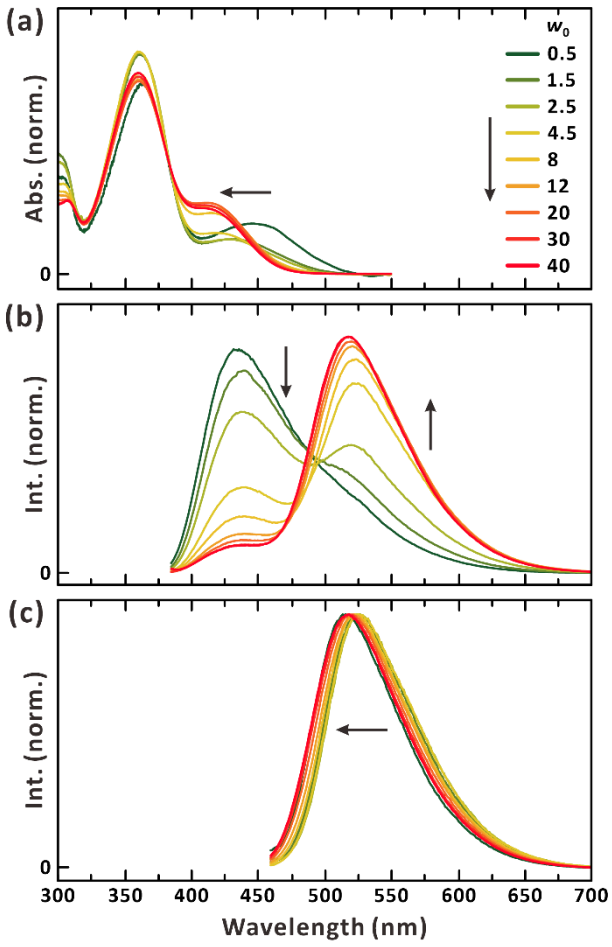

Figure 2. (a) UV/vis absorption spectra and emission spectra with (b) λ_{ex} = 375 nm and (c) λ_{ex} = 450 nm of $NM7HQ^+$ in the water/AOT/*n*-heptane RMs for different w_0 values.

Both emission bands were characterized by shifts in the wavelength of their maxima with increasing water pool size. The overlap of the C band with the blue tail of the Z band in the absorption spectra and the overlap of the red tail of the C* band with the K* band in the emission spectra hampered the precise quantification of these shifts. To extract the spectral shift and amplitude of each band, the absorption and emission spectra were fit using lognormal peak functions. **Figure 3** shows the

deconvolution procedure detailed in **Section 2.3** along with examples of the fits (dotted lines). All spectra were fitted with bi-lognormal peak functions, except for the emission spectra with λ_{ex} = 450 nm and the spectra with w_0 = 0.5 and λ_{ex} = 375 nm; as ESPT cannot occur when photoexciting the ground-state Z with λ_{ex} = 450 nm or without water, only a single emission band corresponding to C* or K* was observed in these spectra.

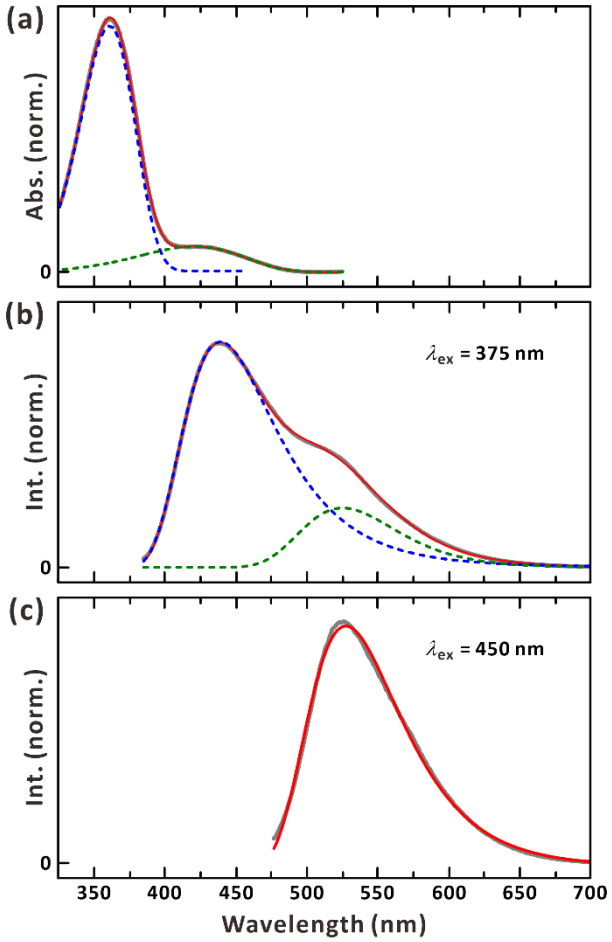

Figure 3. Decomposition of (a) the UV/vis absorption spectra and the emission spectra with (b) λ_{ex} = 375 nm and (c) λ_{ex} = 450 nm when w_0 = 2.5. The red solid lines represent the sum of the individual lognormal distribution fitting curves of the component spectra (dotted lines) and are overlaid on the measured spectra (gray solid).

The relative absorption, relative intensity, and peak position of each band as a function of w_0 are presented in **Figure 4**. The major form of NM7HQ$^+$ in the ground state is C. The fraction of C in the system increased slightly as w_0 was increased from 0.5 to 2.5, and then decreased at $w_0 > 2.5$ (**Figure 4(a)**). The trend indicated that the ground state equilibrium favored the C species with increasing RM size ($w_0 \leq 2.5$). The increasing abundance of water molecules likely provided more ambient (hydrated) protons, which, when coupled with the sufficiently low dielectric constant of the crowded RM interior, favored the efficient ground-state recombination of the protons with Z to regenerate C. In contrast, in

larger water pools ($w_0 > 2.5$) with substantially larger dielectric values (and hence more efficient charge screening), the separation between Z and the hydrated proton became easier and the ground-state recombination of protons with C was hampered, decreasing the fraction of C. In the system with the largest water pool ($w_0 = 40$) the ratio of C was similar to that in the "dry" RMs ($w_0 = 0.5$). In addition, increasing the size of the water pools appeared to induce blue-shifting of the C and Z bands (**Figure 4(b)**). The hypsochromic shift of the absorption bands with increasing solvent polarity indicated that the dipole moments of both prototropic species were higher in their ground states than in their excited states. TDDFT calculations confirmed that the dipole moments of both C and Z were larger in the ground states than in the corresponding excited states (**Figure 5**) [32]. It thus follows that the local environment of the probes became more polar with increasing w_0 [33].

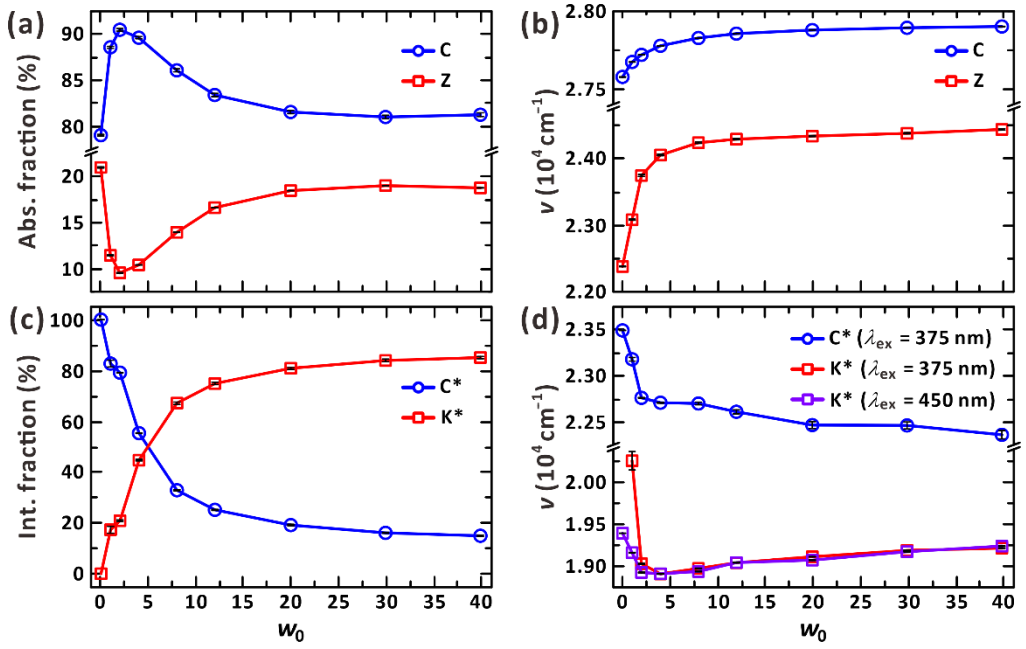

Figure 4. Results of the lognormal fitting of the UV/vis absorption spectra and emission spectra of $NM7HQ^+$ in AOT/*n*-heptane RMs as a function of w_0. (a) Absorption fractions of C and Z. (b) Positions of the maxima of the emission bands of C and Z. (c) Emission intensity fractions of C* and K* at an excitation wavelength of 375 nm. (d) Positions of the maxima of the emission bands of C* and K*.

Figure 4(c) shows the relative intensities of the emission peaks of the two prototropic species as a function of w_0. Because the pK_a* of C* is markedly different from the pK_a of C, the excited and ground state equilibria are very different. A gradual decrease in the C* fraction and concomitant increase in the K* fraction were observed with increasing water pool size, indicating more efficient ESPT due to the greater abundance of labile water molecules. With increasing water pool size, the C* and K* bands initially exhibited bathochromic shifts at $w_0 \leq 4.5$ (**Figure 4(d)**). The increased solvent polarity, explaining the gradual hypsochromic shift of the absorption bands at $w_0 \leq 4.5$, could not account for the opposite trend observed in the emission spectra. This implies that specific interactions, such as those

with the ionic headgroups or water, may influence the stabilization of the excited-state dipole with respect to its ground state in such crowded environments. At $w_0 > 4.5$, the position of the C* band peak remained relatively constant, while the K* band showed a small hypsochromic shift with increasing water pool size. As shown in **Figure 4(d)**. K*, with its greater mobility relative to C*, which remained bound to the AOT headgroups and the substantially larger excited-state dipole moment, seemed to be more sensitive to the increased polarity as the water pool grew. Consequently, the increasing energy gap between its solvent-stabilized ground and excited electronic states resulted in hypsochromically shifted emission. Interestingly, the trend in the shift of the emission maximum of K*was identical regardless of its origin, i.e., whether K* was produced via the ESPT of C* or the Franck–Condon excitation of Z.

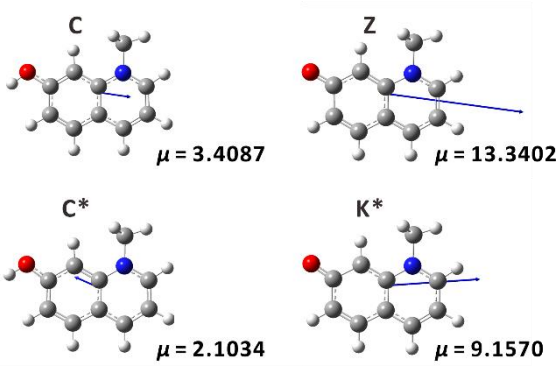

Figure 5. Dipole moment and ball-stick structures of each form of $NM7HQ^+$ in the S_0 and S_1 states as calculated by DFT/TDDFT using the CAM-B3LYP functional with the 6-311G+(d, p) basis sets.

3.2. TRES

We reconstructed the TRES from a series of fluorescence kinetic profiles obtained at 5 nm wavelength intervals. For example, **Figure 6 (a)** depicts the TRES obtained at an excitation wavelength of 375 nm for w_0 = 2.5, 8, and 20. Consistent with the steady-state emission spectra, the contribution of K* originating from C* via ESPT increased with increasing w_0. At w_0 = 2.5, the initial intensity of the C* band at approximately 430nm was more than four times higher than that of the K* band at approximately 520 nm. At w_0 = 8, the initial intensities of the C* and K* bands were comparable, while at w_0 = 20, the K* emission band was more intense than the C* band. These results indicate that in the period shortly after excitation (~100 ps), the conversion of C* to K* was greater in larger water pools. These results are consistent with previous reports where in ESPT was enhanced with increasing w_0 value [9,10]. At the same time, the C* and K* bands showed spectral shifts. The confinement effect of the RM that retards the motion of water molecules and therefore inhibits ESPT, became less effective with the growth of the water pool.

We also obtained a series of TRES with varying w_0 values via excitation at 450 nm to observe

the K* dynamics originating from the Franck–Condon excitation of its ground state (the Z form). These results excluded the effect of the ESPT and could thus be compared with the dynamics of K* originating from C* via the ESPT. **Figure 6(b)** shows the TRES obtained via excitation at 450 nm and w_0 = 2.5, 8, and 20. The resulting TRES showed prominent shifts compared to those obtained using excitation at 375 nm (upper panel). In the λ_{ex} = 375 nm spectra, two overlapping spectral shifts can be observed, but are not clearly resolved. On the other hand, the shift in the peak of K* excited from Z (λ_{ex} = 450 nm) is easily noticeable.

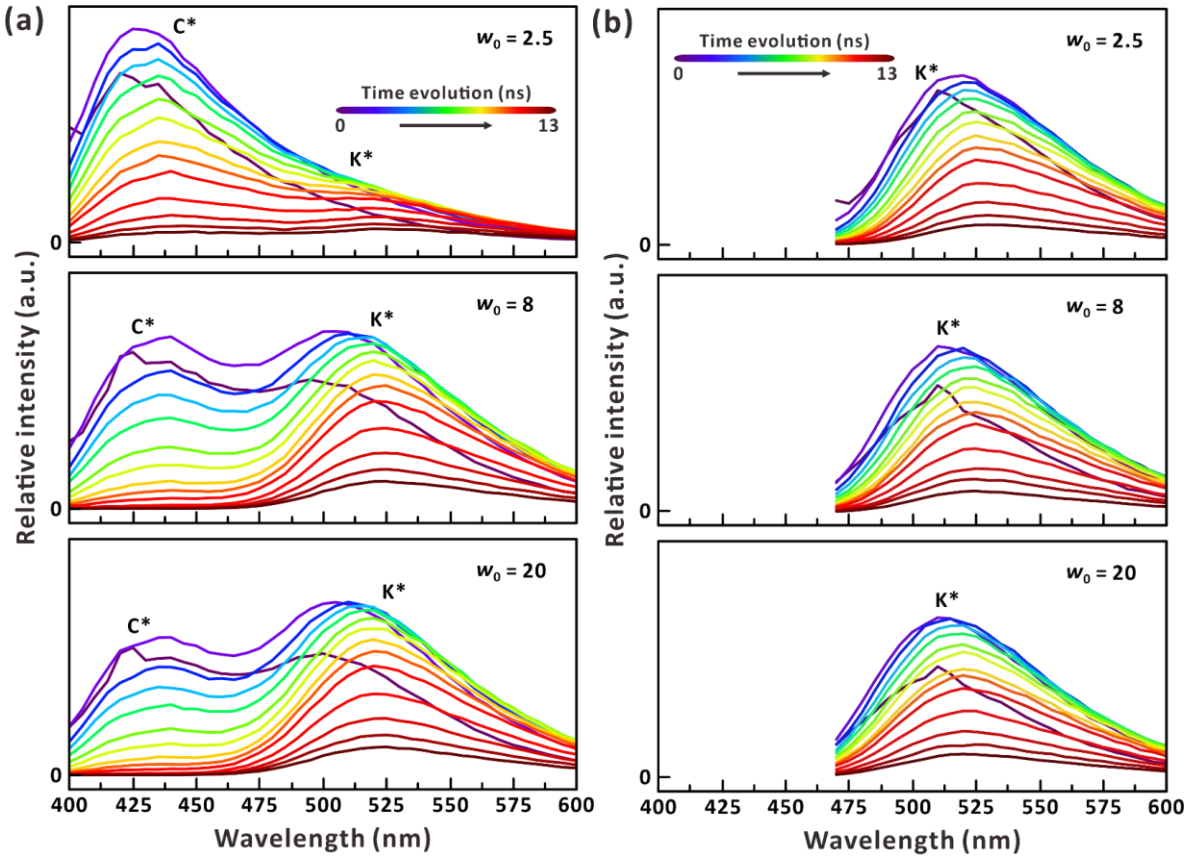

Figure 6. TRES of NM7HQ$^+$ in water/AOT/*n*-heptane RMs with λ_{ex} = 375 nm and (a) w_0 = 2.5, (b) w_0 = 8, and (c) w_0 = 20, and with λ_{ex} = 450 nm and (d) w_0 =2.5, (e) w_0 = 8, and (f) w_0 = 20.

3.3. Spectral deconvolution of TRES

Figure 7 shows a typical deconvolution of the TRES data obtained at λ_{ex} = 375 nm into its component C* and K* spectra. The $v(t)$ profiles for the C* band extracted from the TRES data with λ_{ex} = 375 nm are shown in **Figure 8(a)**, and those of the K* bands obtained with λ_{ex} = 375 nm and 450 nm are shown in **Figure 8(b)** and **(c)**, respectively. The extracted $v(t)$ profiles were fitted to exponential functions, and the fit parameters are listed in **Tables 1–3**. A comparison of the $v(t)$ profiles of the C* and K* emission revealed an abnormally slow-decaying component with a timescale of tens

of nanoseconds in the C* emission at small w_0 values, i.e., $w_0 \leq 2.5$.

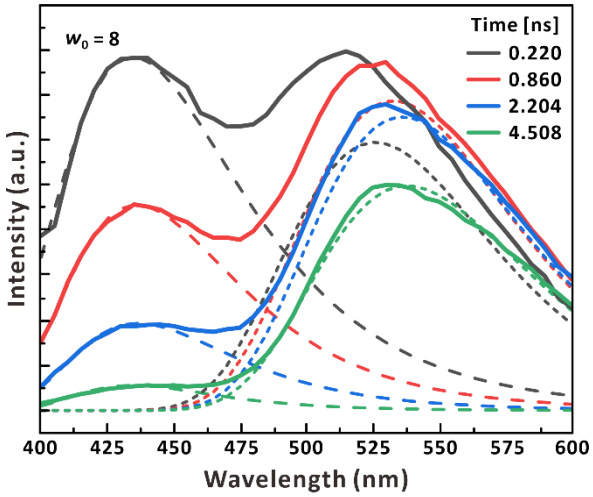

Figure 7. Deconvolution of the TRES of $NM7HQ^+$ in water/AOT/*n*-heptane RMs at w_0 = 8. The long- and short-dashed lines represent the deconvoluted spectra of C* and K*, respectively.

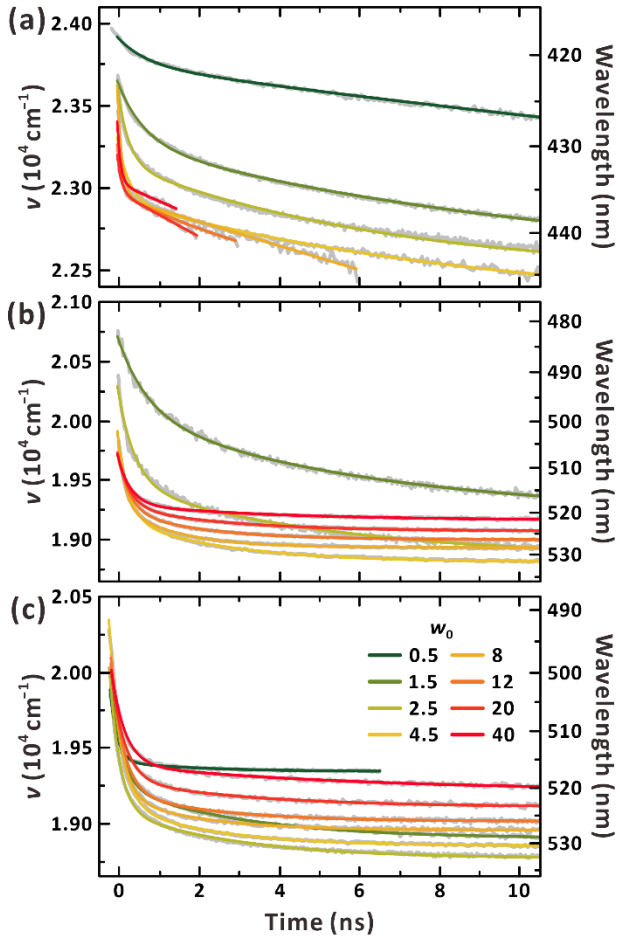

Figure 8. $\nu(t)$ profiles of $NM7HQ^+$ in the water/AOT/*n*-heptane RMs: (a) C* bands and (b) K* bands with λ_{ex} = 375 nm, and (c) K* bands with λ_{ex} = 450 nm for different w_0 values.

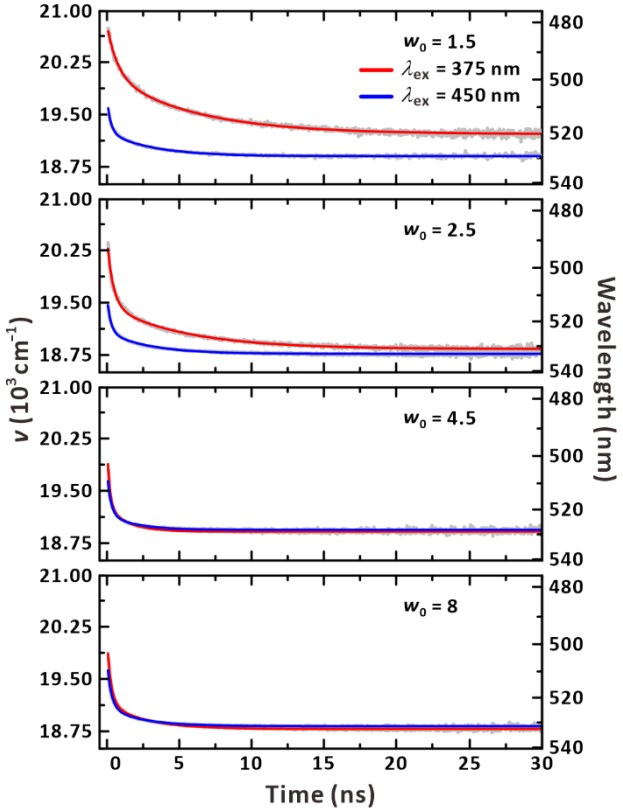

Figure 9. $\nu(t)$ profiles of NM7HQ$^+$ in water/AOT/*n*-heptane RMs for the K* bands at λ_{ex} = 375 nm (red line) and λ_{ex} = 450 nm (blue line) at different w_0 values.

With increasing w_0, the spectral shift occurred on a faster timescale, consistent with the availability of more labile water in the water pool. Additionally, the wavenumber of the emission maximum at infinite time, ν_∞, showed a gradual decrease or red shift with increasing water pool size. In the larger water pools, the fluorescence lifetime of C* became much shorter than the timescale of the spectral shift, and the parameters for the long-lived component could not be accurately determined. The spectral shifts of the K* peaks extracted from the TRES at λ_{ex} = 375 nm and 450 nm were both fitted using biexponential functions, providing two time constants: One of hundreds of picoseconds and the other of a few nanoseconds (**Figure 9**). Although the ν_∞ values obtained from TRES using λ_{ex} = 375 nm and 450 nm were the same within 50 cm^{-1}, the total spectral shift values, i.e., $\nu_1 + \nu_2$, were quite different. The amplitudes of the correlation components showed similar trends; as the size of the water pool was increased, the fraction of the fast component increased while that of the slow component decreased, leading to faster hydration dynamics. With increasing w_0, the spectral relaxations for the fast and slow components of the $\nu(t)$ profiles of the C* band accelerated. In the $\nu(t)$ profiles of K* originating from both C* and Z, at small water pool sizes, the fast and slow time constants became shorter with increasing w_0; this trend was similar to that observed for C*. However, at larger water pool sizes ($w_0 \geq 8$), this trend no longer held. The slow time constant increased with increasing pool size; however, its amplitude decreased, indicating that it contributed less to the overall hydration.

Table 1. Fitting parameters[a] of the $\nu(t)$ functions for the C* bands extracted from TRES with λ_{ex} = 375 nm.

w_0	ν_1 (cm^{-1})	τ_1 (ns)	ν_2 (cm^{-1})	τ_2 (ns)	$\nu_1 + \nu_2$ (cm^{-1})	ν_∞ (cm^{-1})
0.5	165.6 ± 12.6	0.71 ± 0.11	1444 ± 36.8	42.04 ± 1.96	1609.6 ± 38.9	22297 ± 41
1.5	370.2 ± 9.4	0.66 ± 0.03	759.6 ± 3.8	10.67 ± 0.14	1129.9 ± 10.1	22512 ± 2
2.5	467.4 ± 33.1	0.27 ± 0.03	686.3 ± 8.6	6.84 ± 0.16	1153.6 ± 34.2	22460 ± 3
4.5	385.1 ± 27.2	0.29 ± 0.04	666.2 ± 8.8	9.43 ± 0.46	1051.2 ± 28.6	22251 ± 12
8	655.8 ± 25.7	0.12 ± 0.01	N.A.[b]	N.A.[b]	N.A.[b]	N.A.[b]
12	295.1 ± 21.1	0.10 ± 0.01				
20	220.5 ± 11.5	0.10 ± 0.02				
40	367.4 ± 26.2	0.08 ± 0.01				

[a] Determined using Equation (3)

[b] Not available due to the poor S/N ration after 1 ns resulting from the shortened C* lifetimes

Table 2. Fitting parameters[a] of the $\nu(t)$ functions for the K* bands extracted from TRES with λ_{ex} = 375 nm.

w_0	ν_1 (cm^{-1})	τ_1 (ns)	ν_2 (cm^{-1})	τ_2 (ns)	$\nu_1 + \nu_2$ (cm^{-1})	ν_∞ (cm^{-1})
1.5	631.0 ± 15.4	0.73 ± 0.04	852.6 ± 12.4	5.95 ± 0.1	1483.6 ± 19.8	19,221 ± 2
2.5	823.5 ± 15.2	0.42 ± 0.01	622.1 ± 7.6	5.37 ± 0.09	1445.6 ± 17.0	18,842 ± 1
4.5	724.7 ± 21.1	0.27 ± 0.02	365.8 ± 14.3	2.58 ± 0.10	1090.4 ± 25.5	18,813 ± 1
8	631.2 ± 30.7	0.18 ± 0.02	342.4 ± 24.8	1.45 ± 0.10	973.6 ± 39.5	18,935 ± 1
12	482.6 ± 23.1	0.30 ± 0.03	250.0 ± 20.7	2.00 ± 0.14	732.6 ± 31.0	19,001 ± 1
20	434.7 ± 18.6	0.30 ± 0.03	208.1 ± 13.5	2.59 ± 0.16	642.8 ± 23.0	19,073 ± 1
40	423.5 ± 16.3	0.31 ± 0.02	135.6 ± 7.9	3.99 ± 0.27	559.1 ± 18.1	19,161 ± 1

[a] Determined using Equation (3)

Table 3. Fitting parameters[a] of the $\nu(t)$ functions for the K* bands extracted from TRES with λ_{ex} = 450 nm.

w_0	ν_1 (cm^{-1})	τ_1 (ns)	ν_2 (cm^{-1})	τ_2 (ns)	$\nu_1 + \nu_2$ (cm^{-1})	ν_∞ (cm^{-1})
0.5	151.7 ± 8.3	0.17 ± 0.01	61.4 ± 4.7	2.13 ± 0.47	213.2 ± 9.5	19,345 ± 3
1.5	351.3 ± 7.7	0.26 ± 0.01	340.7 ± 5.1	3.11 ± 0.07	692.1 ± 9.2	18,902 ± 1
2.5	393.4 ± 5.1	0.25 ± 0.01	310.1 ± 3.4	2.94 ± 0.05	703.5 ± 6.1	18,771 ± 1
4.5	533.5 ± 22.7	0.28 ± 0.02	271.1 ± 17.2	2.29 ± 0.16	804.6 ± 28.5	18,854 ± 1
8	480.3 ± 38.8	0.25 ± 0.03	222.1 ± 30.4	1.94 ± 0.27	702.4 ± 49.3	18,958 ± 2
12	473.2 ± 6.3	0.29 ± 0.01	197.6 ± 5.0	2.27 ± 0.07	670.8 ± 8.0	19,016 ± 1
20	419.7 ± 23.4	0.33 ± 0.03	177.9 ± 17.6	3.26 ± 0.36	597.6 ± 29.3	19,111 ± 2
40	383.9 ± 14.7	0.33 ± 0.03	171.7 ± 8.7	5.94 ± 0.46	555.6 ± 17.1	19,216 ± 2

[a] Determined using Equation (3)

3.4. Time-resolved fluorescence anisotropy

The time-resolved fluorescence anisotropy, $r(t)$, of $NM7HQ^+$ in the RMs was measured via excitation at 375 nm and 450 nm. **Figure 10(a)** and **(b)** shows the anisotropy decay profiles of C* and K* monitored at 440 nm and 550 nm, after excitation at 375 nm. All the profiles were fitted to bi-exponential functions except for those at $w_0 = 0.5$, which were fitted to a single-exponential function. The fitting parameters are listed in **Tables 4–6**.

The rates of the depolarization processes for both C* and K* were higher in the larger RMs. The observation of two anisotropy components for C* and K* indicated the presence of two distinct depolarization processes. For K*, with increasing w_0, the amplitude of the slow component, A_{slow}, decreased, while that of the fast component, A_{fast}, concomitantly increased. This indicated that a greater fraction of the fast component facilitated the overall depolarization. Meanwhile, for C*, while A_{slow} decreased with increasing pool size, A_{slow} remained the major component at all water pool sizes. The trend in the fast depolarization of K* was also observed in the anisotropy decay profiles monitored at 550 nm with excitation at 450 nm (**Figure 10(c)**). The major difference in the decays of the anisotropy of K* originating from C via ESPT and from Z via Franck–Condon excitation (λ_{ex} = 375 and 450 nm, respectively) was the initial anisotropy values (r_0). The discrepancy can be rationalized as follows. ESPT changes the dipole moment of $NM7HQ^+$ substantially in the excited state by transforming C* into K*. Our TDDFT calculations of the excited state C* and K* forms of $NM7HQ^+$ suggested that deprotonation induces changes in the direction and strength of the dipole moments, as shown in **Figure 5**. Consequently, during the early time window of ESPT (<100 ps), the charge distribution is altered drastically, and the ultrafast depolarization component remains undetected (beyond IRF).

Table 4. Bi-exponential fitting parameters (single-exponential decay parameters for $w_0 = 0.5$) of the fluorescence anisotropy of $NM7HQ^+$ in water/AOT/*n*-heptane RMs at different w_0 values, monitored at 440 nm with λ_{ex} = 375 nm.

w_0	r_0	τ_{fast} (ns)	A_{fast} (%)	τ_{slow} (ns)	A_{slow} (%)
0.5	0.33 ± 0.01			1.72 ± 0.02	100
1.5	0.34 ± 0.01	0.21 ± 0.05	13.7 ± 1.6	2.06 ± 0.03	86.3 ± 1.0
2.5	0.36 ± 0.01	0.16 ± 0.02	26.1 ± 1.9	2.22 ± 0.04	73.9 ± 0.9
4.5	0.33 ± 0.01	0.26 ± 0.05	35.9 ± 3.3	2.31 ± 0.11	64.1 ± 2.4
8	0.32 ± 0.03	0.19 ± 0.07	36.7 ± 6.9	1.67 ± 0.14	63.3 ± 5.0
12	0.32 ± 0.04	0.13 ± 0.08	35.3 ± 10.7	1.36 ± 0.16	64.7 ± 6.7
20	0.30 ± 0.05	0.18 ± 0.13	34.8 ± 13.1	1.38 ± 0.23	65.2 ± 10.8
30	0.29 ± 0.05	0.17 ± 0.14	33.6 ± 13.8	1.29 ± 0.22	66.4 ± 11.8
40	0.31 ± 0.06	0.13 ± 0.10	36.5 ± 14.3	1.10 ± 0.20	63.5 ± 11.7

Table 5. Bi-exponential fitting parameters (single-exponential decay parameters for w_0 = 0.5) of the fluorescence anisotropy of NM7HQ$^+$ in water/AOT/*n*-heptane RMs at different w_0 values, monitored at 550 nm with λ_{ex} = 375 nm.

w_0	r_0	τ_{fast} (ns)	A_{fast} (%)	τ_{slow} (ns)	A_{slow} (%)
0.5	0.30 ± 0.01			1.43 ± 0.01	100
1.5	0.30 ± 0.05	0.37 ± 0.02	38.4 ± 1.6	1.55 ± 0.03	61.6 ± 1.7
2.5	0.27 ± 0.01	0.28 ± 0.01	46.7 ± 1.7	1.22 ± 0.03	53.3 ± 1.8
4.5	0.24 ± 0.07	0.21 ± 0.01	61.0 ± 2.6	0.83 ± 0.04	39.0 ± 2.8
8	0.24 ± 0.01	0.17 ± 0.01	76.2 ± 3.2	0.67 ± 0.06	23.8 ± 3.5
12	0.22 ± 0.01	0.18 ± 0.01	85.2 ± 2.2	0.89 ± 0.10	14.8 ± 2.3
20	0.21 ± 0.01	0.19 ± 0.04	93.6 ± 1.1	4.14 ± 0.04	6.4 ± 0.4
30	0.18 ± 0.01	0.18 ± 0.01	93.6 ± 1.3	2.83 ± 0.29	6.4 ± 0.6
40	0.19 ± 0.01	0.18 ± 0.01	95.3 ± 1.2	3.61 ± 0.05	4.7 ± 0.5

Table 6. Bi-exponential fitting parameters (single-exponential decay parameters for w_0 = 0.5) of the fluorescence anisotropy of NM7HQ$^+$ in water/AOT/*n*-heptane RMs at different w_0 values, monitored at 550 nm with λ_{ex} = 450 nm.

w_0	r_0	τ_{fast} (ns)	A_{fast} (%)	τ_{slow} (ns)	A_{slow} (%)
0.5	0.33 ± 0.01			1.72 ± 0.02	100
1.5	0.36 ± 0.01	0.21 ± 0.02	17.6 ± 0.9	2.29 ± 0.03	82.3 ± 0.6
2.5	0.35 ± 0.01	0.28 ± 0.02	34.4 ± 2.5	2.04 ± 0.04	65.6 ± 1.0
4.5	0.35 ± 0.01	0.36 ± 0.01	67.5 ± 1.4	2.01 ± 0.10	32.5 ± 1.3
8	0.34 ± 0.04	0.25 ± 0.01	79.9 ± 1.2	1.62 ± 0.10	20.1 ± 1.2
12	0.33 ± 0.01	0.24 ± 0.01	83.5 ± 1.2	1.74 ± 0.12	16.5 ± 1.1
20	0.31 ± 0.01	0.21 ± 0.01	86.1 ± 1.4	1.23 ± 0.12	13.9 ± 1.4
30	0.27 ± 0.04	0.21 ± 0.01	88.2 ± 1.4	1.43 ± 0.18	11.8 ± 1.3
40	0.25 ± 0.01	0.18 ± 0.01	88.9 ± 1.7	1.25 ± 0.19	11.1 ± 1.7

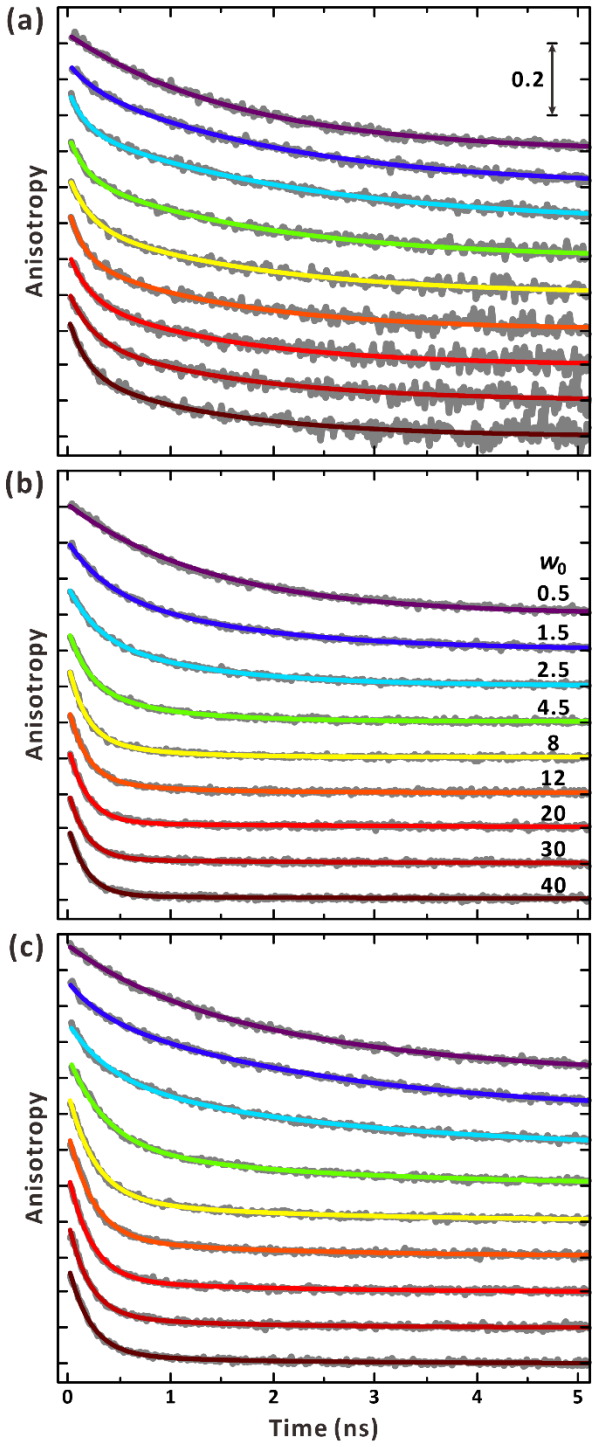

Figure 10. Fluorescence anisotropy decay profiles with λ_{ex} = 375 nm monitored at (a) 450 nm and (b) 550 nm, and (c) the profiles with λ_{ex} = 450 nm monitored at 550 nm of $NM7HQ^+$ in the water/AOT/*n*-heptane RMs at different w_0 values.

IV. Discussion

4.1. Location of $NM7HQ^+$

As presented in the Results section, the depolarization dynamics of photoexcited $NM7HQ^+$ in the water pools exhibited two distinct components. Here, we apply the well-known wobbling-in-a-cone model to our observations to explain the superimposed depolarization dynamics [33]. According to this two-component model, the fast and slow anisotropy decay components can be treated separately, and the total rotation correlation function, $C_r(t)$, can be expressed as the product of slow and fast correlation functions as follows:

$$C_r(t) = C_{\text{fast}}(t) \cdot C_{\text{slow}}(t) \tag{4}$$

The slow correlation function, $C_{\text{slow}}(t)$, can be represented as a single exponential function,

$$C_{\text{slow}}(t) = e^{-t/\tau_{\text{slow}}}, \tag{5}$$

where the slow depolarization time, τ_{slow}, results from two different isotropic motions: The rotation of the entire micellar assembly and the lateral diffusion of the fluorescent probe at the interfacial region between the AOT headgroups and the water pool. Accordingly, the total slow time constant can be expressed as

$$\frac{1}{\tau_{\text{slow}}} = \frac{1}{\tau_{\text{M}}} + \frac{1}{\tau_{\text{L}}}, \tag{6}$$

where τ_{M} is the rotation time of the entire RM and τ_{L} is the lateral diffusion time of the probe in the RMs [33]. τ_{M} can be calculated using the Stokes-Einstein equation:

$$\tau_{\text{M}} = \frac{4\pi\eta r_{\text{h}}^3}{3kT}, \tag{7}$$

where η is the viscosity of the non-polar solvent, k is the Boltzmann constant, T is the temperature in Kelvin, and r_{h} is the hydrodynamic radius of the RM. r_{h} is given by its linear relationship with the water pool size as [34].

$$r_{\text{h}} = r_{\text{wp}} + 1.0 \text{ nm}, \tag{8}$$

where r_{wp} is the radius of the water pool in the RMs and is proportional to the w_0 values according to [35]:

$$2r_{\text{wp}} = 0.29w_0 + 1.1 \text{ nm} \tag{9}$$

In our system, because the interfacial region is negatively charged (due to the sulfonate moiety

of the AOT headgroup), depolarization via the rotational diffusion of the cationic probe is heavily restricted. Consequently, the fast rotation correlation function, $C_{fast}(t)$, can be expressed as [31]:

$$C_{fast}(t) = \beta + (1 - \beta)\, e^{-t/\tau_w}, \tag{10}$$

where β is a factor determining how strictly the probes are bound to the interfacial layers. The more closely β approaches 1, the more tightly bound the probes are, and therefore, the lower the contribution of the fast component to the overall depolarization process is. β is the square of the order parameter S, which is related to the wobbling cone angle, θ_c, in the wobbling-in-a-cone model as [33]:

$$\beta = S^2 = \left[\frac{1}{2}\cos\theta_c(1+\cos\theta_c)\right]^2 \tag{11}$$

In the wobbling-in-a-cone model, a probe is bound to a layer, so it cannot rotate freely, but instead wobbles within a hypothetical cone with a wobbling time constant, τ_w. θ_c signifies how freely the bound molecules can move. Finally, the overall anisotropy decay can be formulated as [36–41]:

$$r(t) = r_0 C_r(t) = r_0\left[(1 - \beta)e^{-t/(\tau_M^{-1}+\tau_L^{-1}+\tau_w^{-1})} + \beta e^{-t/(\tau_M^{-1}+\tau_L^{-1})}\right] \tag{12}$$

Tables 7–9 list the parameters obtained from the above analyses for different w_0 values. Our analyses revealed that increasing the water pool size induced a decrease in S. It follows that for larger water pools, the curvature of the spherical interfacial layer of AOT became shallower, and the binding force confining the $NM7HQ^+$ molecules became weaker, resulting in larger θ_c values. A comparison of C* and K* shows that in small water pools ($w_0 \leq 2.5$), both C* and K* had small θ_c values. As the water pool was expanded, the θ_c value for C* converged to 30°, while the corresponding values for K* converged to 60°–70°. These results are consistent with the rotational freedom expected for the probe in its different charge states. Prior to ESPT, C* has a positive formal charge and would be expected to be strongly bound to the negatively charged AOT headgroups through electrostatic interactions. During the ESPT, C* donates its proton to water and transforms into the neutral K* form. This changes the interactions between the AOT headgroups and the probe from the strong ion–ion interactions into weaker ion–dipole interactions. The loosely bound K* form probe, with its greater degrees of freedom, is thus able to wobble over a wider space, resulting in the larger θ_c values in larger water pools. It also follows that K*was no longer restricted to the interface region, and was pushed toward the water pool, where the environment is more labile. Thus, in terms of location, one may envisage a scenario in which C* is tightly bound to the interface layer and hence remains partially hydrated, while K* obtains a full hydration (by bound water) shell in its proximity.

This conclusion was cross-checked by comparing the lateral diffusion times, τ_L, and the corresponding lateral diffusion coefficients, D_L, of the two forms of the probe. The τ_L values were

calculated using Equation (6), and were used to obtain the D_L values via the following equation [37]:

$$D_L = \frac{r_{wp}^2}{6\tau_L} \quad (13)$$

As presented in **Tables 7** and **9**, the D_L values for C* and K* increased from 3.7×10^{-11} m^2 s^{-1} to 6.1×10^{-9} m^2 s^{-1}, and from 5×10^{-11} m^2 s^{-1} to 5.3×10^{-9} m^2 s^{-1}, respectively, when the w_0 value was increased from 4.5 to 40. In larger water pools, the depolarization of both C* and K* was facilitated via lateral diffusion. The trend in the D_L values of K* formed from C* via ESPT with increasing w_0 (**Table 8**) was similar. The D_L value gradually increased from 1.72×10^{-10} m^2 s^{-1} to 8.2×10^{-9} m^2 s^{-1} as the w_0 value was increased from 4.5 to 40. Interestingly, these D_L values were typically larger (within the error range) than those of C* (**Tables 7 and 8**). This can be attributed to the ESPT-induced diffusion of the probe. At the moment of photoexcitation, C* is initially tightly bound to the sulfonate moieties of the AOT headgroups. It then loses a proton via ESPT and is transformed into the neutral species K*. Due to its altered charge state, K* is no longer constrained to the anionic interface and can diffuse toward the core of the water pool. This additional radial diffusion resulted in the larger overall D_L for K* originating from C compared to that of K* originating from Z.

The wobbling diffusion coefficient, D_w, for the probe was calculated using the following equation [36]:

$$D_w = \frac{1}{[(1 - S^2)\tau_w]}\left[\left\{\frac{x^2(1+x)^2}{2(x-1)}\right\}\left\{\log\left(\frac{1+x}{2}\right) + \frac{(1-x)}{2}\right\} + \frac{(1-x)}{24}(6 + 8x - x^2 - 12x^3 - 7x^4)\right] \quad (14)$$

where x is cos θ_c. The τ_w values of C* in **Table 7** are similar regardless of the w_0 value. This indicates that C* experienced similar restriction in its motion at the vicinity of the sulfonate moiety in all cases. The wobbling cone angle gradually increased from 18° at w_0 = 1.5 to 31° at w_0 = 4.5 and then remained nearly constant as w_0 was increased to 40. The corresponding θ_c values were consistently higher for K* (**Tables 7**, **8**, and **9**). Although the τ_w values of C* did not differ greatly from those of K*, the latter exhibited larger D_w values that generally increased with increasing water pool size. The larger D_w values with larger wobbling cone angles but similar wobbling time constants suggested that K* swept out a larger volume during its wobbling but experienced less friction than C*. This is consistent with the fact that the greater abundance of water molecules with the growing pool size reduces the local micro-viscosity around K*, leading to an overall enhancement of its wobbling mobility. A comparison of the wobbling parameters of K* generated via the ESPT of C* and those of K* generated from the direct Franck–Condon excitation of Z (**Tables 8** and **9**) indicated that the θ_c and D_w values tended to be slightly higher for K* generated from C*, implying slightly increased mobility as a consequence of the ESPT-assisted diffusion.

Table 7. The parameters of the wobbling in a cone model with λ_{ex} = 375 nm monitored at 440 nm.

w_0	S[a]	θ_c[b] (°)	τ_w[c] (ns)	D_w[d] (10^8 s^{-1})	d_{wp}[e] (nm)	r_h[f] (nm)	τ_M[g] (ns)	τ_L[h] (ns)	D_L[i] (10^{-10} m^2 s^{-1})
0.5	N.A.[j]	N.A.[j]	N.A.[j]	N.A.[j]	1.10	1.55	1.81	N.A.[j]	N.A.[j]
1.5	0.93 ± 0.01	17.81 ± 0.12	0.23 ± 0.03	1.20 ± 0.25	1.39	1.70	1.93	N.A.[k]	N.A.[k]
2.5	0.86 ± 0.01	25.43 ± 0.01	0.17 ± 0.02	3.22 ± 0.30	1.68	1.84	2.46		
4.5	0.80 ± 0.02	30.59 ± 0.02	0.28 ± 0.04	2.68 ± 0.33	2.26	2.13	3.82	5.82 ± 0.28	0.37 ± 0.02
8	0.80 ± 0.04	31.04 ± 0.04	0.21 ± 0.06	3.71 ± 0.94	3.42	2.71	7.87	2.11 ± 0.18	2.31 ± 0.2
12	0.81 ± 0.05	30.21 ± 0.06	0.14 ± 0.07	5.33 ± 2.09	4.58	3.29	14.1	1.50 ± 0.17	5.84 ± 0.67
20	0.81 ± 0.08	30.04 ± 0.08	0.20 ± 0.11	3.63 ± 2.16	6.90	4.45	34.9	1.44 ± 0.24	13.79 ± 2.26
30	0.81 ± 0.09	29.58 ± 0.09	0.20 ± 0.12	3.49 ± 2.44	9.80	5.90	81.2	1.32 ± 0.23	30.31 ± 5.37
40	0.80 ± 0.08	30.81 ± 0.09	0.15 ± 0.09	5.19 ± 3.09	12.7	7.35	157.0	1.10 ± 0.20	61.11 ± 10.91

[a] S = order parameter.
[b] θ_c = cone angle.
[c] τ_w = wobbling time constant.
[d] D_w = wobbling diffusion coefficient.
[e] d_{wp} = diameter of water pool.
[f] r_h = radius of RM.
[g] τ_m = entire micelle rotation time constant.
[h] τ_L = lateral diffusion time constant.
[I] D_L = lateral diffusion coefficient.
[j] Not available, single exponential fitting function was used for w_0 = 0.5 where the wobbling-in-a-cone model cannot be invoked.
[k] Not available, because in the small water pools (w_0 = 1.5-2.5), estimation of the lateral diffusion constant and coefficient becomes erroneous.

Table 8. The parameters of the wobbling in a cone model with λ_{ex} = 375 nm monitored at 550 nm.

w_0	S[a]	θ_c[b] (°)	τ_w[c] (ns)	D_w[d] (10^8 s^{-1})	d_{wp}[e] (nm)	r_h[f] (nm)	τ_M[g] (ns)	τ_L[h] (ns)	D_L[i] (10^{-10} m^2 s^{-1})
0.5	N.A.[j]	N.A.[j]	N.A.[j]	N.A.[j]	1.10	1.55	1.81	N.A.[j]	N.A.[j]
1.5	0.81 ± 0.01	29.97 ± 0.01	0.43 ± 0.02	1.76 ± 0.16	1.39	1.70	1.93	N.A.[k]	N.A.[k]
2.5	0.73 ± 0.01	36.30 ± 0.01	0.37 ± 0.01	2.78 ± 0.18	1.68	1.84	2.46		
4.5	0.59 ± 0.01	45.95 ± 0.01	0.29 ± 0.01	5.19 ± 0.22	2.26	2.13	3.82	1.23 ± 0.07	1.72 ± 0.1
8	0.45 ± 0.01	54.8 ± 0.01	0.22 ± 0.01	8.6 ± 0.22	3.42	2.71	7.87	0.87 ± 0.08	5.59 ± 0.54
12	0.39 ± 0.01	59.05 ± 0.01	0.23 ± 0.01	9.22 ± 0.18	4.58	3.29	14.1	0.92 ± 0.12	9.45 ± 1.25
20	0.3 ± 0.01	64.86 ± 0.01	0.2 ± 0.01	11.32 ± 0.09	6.90	4.45	34.9	1.26 ± 0.24	15.72 ± 2.96
30	0.28 ± 0.01	66.19 ± 0	0.19 ± 0.11	12.45 ± 0.07	9.80	5.90	81.2	1.62 ± 0.28	24.67 ± 4.33
40	0.32 ± 0.01	63.69 ± 0.01	0.2 ± 0.01	11.49 ± 0.17	12.7	7.35	157.0	0.82 ± 0.17	81.79 ± 16.91

[a] S = order parameter.
[b] θ_c = cone angle.
[c] τ_w = wobbling time constant.
[d] D_w = wobbling diffusion coefficient.
[e] d_{wp} = diameter of water pool.
[f] r_h = radius of RM.
[g] τ_m = entire micelle rotation time constant.
[h] τ_L = lateral diffusion time constant.
[I] D_L = lateral diffusion coefficient.
[j] Not available, single exponential fitting function was used for w_0 = 0.5 where the wobbling-in-a-cone model cannot be invoked.
[k] Not available, because in the small water pools (w_0 = 1.5-2.5), estimation of the lateral diffusion constant and coefficient becomes erroneous.

Table 9. The parameters of the wobbling in a cone model with λ_{ex} = 450 nm monitored at 550 nm.

w_0	S[a]	θ_c[b] (°)	τ_w[c] (ns)	D_w[d] (10^8 s^{-1})	d_{wp}[e] (nm)	r_h[f] (nm)	τ_M[g] (ns)	τ_L[h] (ns)	D_L[i] (10^{-10} m^2 s^{-1})
0.5	N.A.[j]	N.A.[j]	N.A.[j]	N.A.[j]	1.10	1.55	1.81	N.A.[j]	N.A.[j]
1.5	0.91 ± 0.01	20.45 ± 0.01	0.24 ± 0.02	1.5 ± 0.13	1.39	1.70	1.93	N.A.[k]	N.A.[k]
2.5	0.81 ± 0.01	29.78 ± 0.01	0.33 ± 0.02	2.21 ± 0.11	1.68	1.84	2.46		
4.5	0.57 ± 0.01	47.22 ± 0.01	0.44 ± 0.01	3.57 ± 0.07	2.26	2.13	3.82	4.24 ± 0.21	0.50 ± 0.02
8	0.45 ± 0.01	55.21 ± 0.00	0.3 ± 0.01	6.44 ± 0.07	3.42	2.71	7.87	2.04 ± 0.13	2.39 ± 0.15
12	0.41 ± 0.01	57.98 ± 0.00	0.28 ± 0.01	7.32 ± 0.06	4.58	3.29	14.1	1.77 ± 0.14	4.93 ± 0.38
20	0.37 ± 0.01	60.12 ± 0.01	0.26 ± 0.01	8.26 ± 0.08	6.90	4.45	34.9	1.27 ± 0.12	15.59 ± 1.51
30	0.34 ± 0.01	62.1 ± 0.01	0.24 ± 0.01	9.26 ± 0.07	9.80	5.90	81.2	1.45 ± 0.18	27.55 ± 3.40
40	0.33 ± 0.01	62.79 ± 0.01	0.25 ± 0.01	8.80 ± 0.09	12.7	7.35	157.0	1.26 ± 0.19	53.35 ± 7.90

[a] S = order parameter.
[b] θ_c = cone angle.
[c] τ_w = wobbling time constant.
[d] D_w = wobbling diffusion coefficient.
[e] d_{wp} = diameter of water pool.
[f] r_h = radius of RM.
[g] τ_m = entire micelle rotation time constant.
[h] τ_L = lateral diffusion time constant.
[I] D_L = lateral diffusion coefficient.
[j] Not available, single exponential fitting function was used for w_0 = 0.5 where the wobbling-in-a-cone model cannot be invoked.
[k] Not available, because in the small water pools (w_0 = 1.5-2.5), estimation of the lateral diffusion constant and coefficient becomes erroneous.

4.2. Hydration in the water pool

The solvation process in the water pool was analyzed via the $v(t)$ profiles extracted from the TRES. The time-dependent Stokes' shift of C* was not completed within our time window (~20 ns) for small w_0 values, indicating the inefficient solvation of C*. As discussed above, C* was tightly bound to the ionic interface, and thus, its overall dipole relaxation was affected not only by water molecules, but also by the AOT headgroups [42]. Because the motion of the sulfonate groups attached to the long-tailed hydrocarbon moieties was much slower than that of the water molecules, the very slow (tens of nanoseconds) component was assigned to the solvation of C* by the headgroups. The additional water in the larger RMs acted as a lubricant to reduce the friction among the headgroups and increase their mobility. The formation of hydration shells around the AOT headgroups in larger water pools also induced partial charge screening from the ambient counter cations (Na^+), further increasing the mobility of the headgroups and interfacial water. The fast component of the $v(t)$ profiles (τ_1, hundreds of picoseconds) was attributed to the hydration dynamics of the AOT-bound interfacial water. The hydration of a probe in bulk water is known to occur within a few picoseconds [27]. However, in RM, the hydrogen-bond network at the AOT interface is strongly disrupted, and the interfacial water remains strongly bound to the sulfonate moieties of the AOT headgroups. This results in a decrease in the orientational motion of the water molecules by several orders of magnitude. The trend in the τ_1 (fast component) of C* was consistent with the constrained nature of the interfacial water. Because the water molecules solvating C* are less congested and arranged along a shallower curvature in RMs with larger water pools, they can move more freely than in the smaller RMs. This was reflected in the gradual decrease in τ_1 with increasing RM water pool size. The changes in the spectral shift (v_1)—representing the relaxation energy of hydration, indicated that from w_0 = 0.5 to 2.5, the addition of water induced substantial solvent relaxation due to the greater abundance of water molecules necessary to solvate C*. Further addition of water reduced v_1. This can be rationalized by the fact that, with the growth of the water pool and thus the fraction of free water, C* starts being influenced by the bulk-like water; the hydration in bulk water is expected to be much faster than the IRF of this study. In addition, the ESPT process responsible for the depopulation of C* began to compete with fast solvation such that a fraction of the v_1 component became unresolvable.

In the case of the $v(t)$ profiles of K* originating from C (λ_{ex} = 375 nm, **Figure 8(b)** and **Table 2**) and Z (λ_{ex} = 450 nm, **Figure 8(c)** and **Table 3**), the time-dependent Stokes' shifts were completed within our measurement period. As shown in **Figure 8**, the hydration of K* was faster than that of C*. The binding effect of the sulfonate group was weaker for K* than C*; this apparently allowed an intervening layer of water molecules to be accommodated between the AOT interface and K*. The observed biphasic solvation process can hence be rationalized as follows: the component with a time constant of several hundred picoseconds (τ_1) originates from the hydration of the probe by water molecules located relatively farther from the AOT interface and closer to the core of the water pool,

while the slower component with a time constant of a few nanoseconds (τ_2) results from hydration of the probe by water molecules bound to the AOT headgroups. We note that the latter component is at least an order of magnitude faster than the slowest component (solvation by headgroups, τ_2) observed for C* (**Table 1**). The component v_1 contributed more to the total spectral relaxation for all water pool sizes, implying that the relatively free water molecules toward the core of the RM made a greater contribution to the overall solvation dynamics of K* than the bound water molecules (**Table 2**). This argument is coherent with the picture established for the location of the probes based on the anisotropy studies.

The dependence of the early time spectral-shift component (v_1) of K* generated through the Franck–Condon excitation of Z on the water pool size showed a similar trend to that of C* (**Tables 1** and **3**). This component initially increased with the water pool size ($w_0 \leq 4.5$) due to the abundance of more labile water. For larger water pools ($8 \leq w_0 \leq 40$), the fraction of free water increased substantially, expediting the hydration. However, some of this ultrafast solvation could not be detected within our IRF; the fraction of undetected solvation was expected to increase with the size of the water pool. Consequently, the net detected v_1 component decreased with increasing pool size ($8 \leq w_0 \leq 40$). Compared to that of C*, the reduction in the v_1 value for K* was much smaller, because the K* population was not depleted by ESPT. The apparent trend in the slower spectral shift component, v_2, (except at $w_0 = 0.5–1.5$) was different from that of v_1; v_2 decreased monotonically with increasing water pool size (**Table 3**). This implied that the contribution of v_2, i.e., the contribution of the headgroup-bound slow water, became less significant as the water pool size was increased, and more labile water became available. Interestingly, for the larger water pools ($8 \leq w0 \leq 40$), the slow time constant (τ_2) gradually increased with the water pool size for both K* cases (**Tables 2** and **3**), albeit with decreasing amplitude. In these cases, the slow headgroup-bound water molecules were likely also engaged in hydrating the ambient counterions (Na^+) near the AOT interface; this competitive solvation would result in K* experiencing a progressively slower τ_2 component.

The local pH around a photoacid immediately after photoexcitation is expected to be higher than bulk due to the residence of the ejected proton in its vicinity. With time, as the proton and the conjugate base solvate and diffuse apart, the pH recovers to the value in bulk, the course of which may contribute to the solvation process accompanying spectral shift. For pyranine, the recovery has been reported to occur in ~0.6 ns in bulk water and a few nanoseconds in hydrogel and micelles [43]. Although the order of the reported values is the same as that of τ_2 in **Table 2**, such values are also observed even when no ESPT is involved (**Table 3**). This suggests that the time-dependent Stokes' shift in this study arises mainly from solvation, rather than the evolution of local pH.

A comparison of the $v(t)$ fit parameters for K* populated via the ESPT of C* and K* produced by the direct photoexcitation of Z indicated that the v_∞ values tended to be similar for a given water pool size, especially at larger pool sizes (**Tables 2** and **3**). It follows that in both cases, K* relaxes to

fully solvated states whose emissive energies, and by implication environments, are similar. As expected, the total spectral shifts, $v_1 + v_2$, of K* were different in the two cases when the water pool is small ($1.5 \leq w_0 \leq 4.5$). Because the local heterogeneity in such crowded environments varies greatly over short distances, the probe location determined the initial, detectable emissive energies of K* and hence, the magnitude of the total spectral shift. Due to the lack of sufficient mobile water, the differences between the final v_∞ values persisted on long time scales (~30 ns, **Figure 9**). When the water pool size reached $w_0 = 4.5$ or larger, the solvation dynamics for both cases converged. The transverse (concentric) radial diffusion time of the K* originating from C* at the interface to the inner residence site of Z could be estimated from the w_0-dependent difference in the solvation dynamics (**Figure 9**). For $w_0 = 1.5$, the probe was nearly immobile, and did not reach the inner site within the detectable time window of 30 ns; that is, the solvation-induced relaxed energy for the K* produced from C* did not reach that of K* produced directly from Z. As the pool size grew, the transverse diffusion accelerated; for example, the relaxation energies for both the cases merged within tens of nanoseconds at $w_0 = 2.5$ and 4.5. When the interface was fully hydrated and free water had started to form at $w_0 = 4.5$ and 8, the apparent solvation dynamics were the same after 700 ps and 250 ps, respectively. From the diffusion coefficients D_L of 1.7×10^{-10} m^2 s^{-1} and 5.6×10^{-10} m^2 s^{-1} for w_0 values of 4.5 and 8, respectively, the root-mean-square displacements were calculated to be approximately 3.5 Å using the relationship $\langle x_2 \rangle^{1/2} = \sqrt{2DT}$ and assuming that the transverse diffusion was governed by the same local viscosity as the lateral diffusion; this distance corresponds to more than one layer of water molecules. For the largest water pool ($w_0 = 40$), the final v_∞ value for hydrated K* generated via the ESPT of C* was even slightly lower in energy than that of K* created via the Franck–Condon excitation of Z (data not shown). This extra stabilization of K* may have originated from the effect of the large polarizable iodide counterion, which would be expected to remain in the vicinity of the cationic C* as it transforms into K* via the ESPT.

Finally, it can be inferred that when C* loses a proton to the surrounding water molecules to generate K*, the resulting K* tends to diffuse slightly from the original bound location toward the core of the water pool in order to minimize the free energy (**Figure 11**). The weaker electrostatic pull from the anionic headgroups, in tandem with the radial polarity and viscosity gradients across the water pool, appear to be the main driving forces behind this concentric radial diffusion.

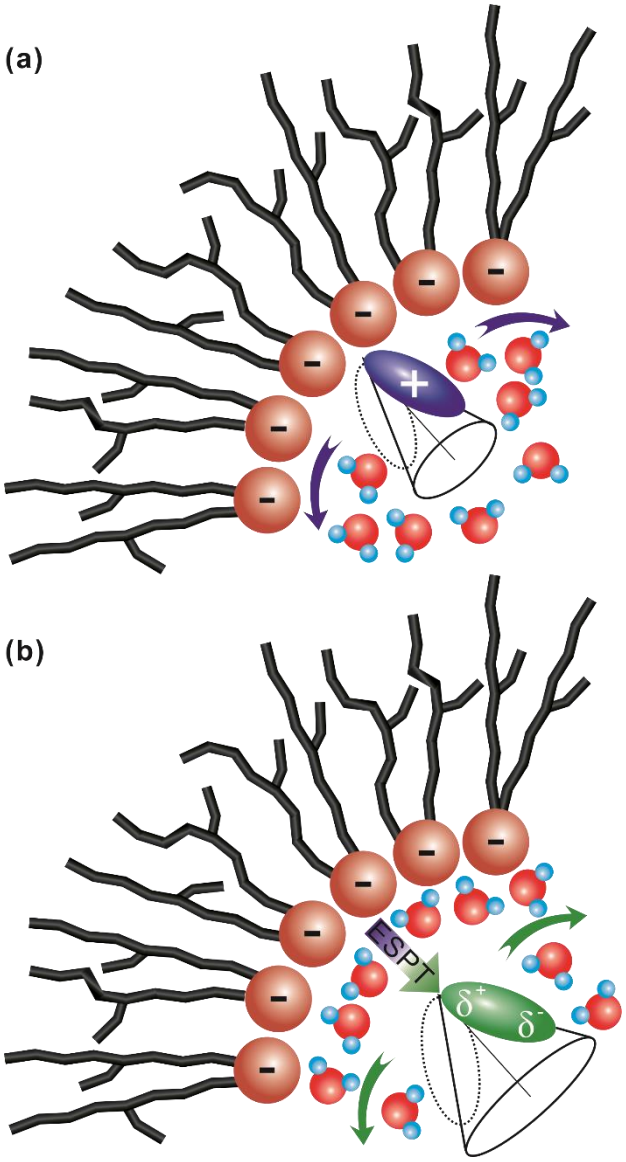

Figure 11. Schematic depicting the rotational motion and hydration of $NM7HQ^+$ following ESPT-assisted diffusion within the water/AOT/*n*-heptane RM for the (a) C*- and (b) K*-form probes.

V. Conclusions

In the present study, we investigated the local environments of the nanosized water pool in the water/AOT/*n*-heptane reverse micellar system. The dynamics were revealed through the steady-state spectra, TRES, and rotational anisotropy of a probe molecule. The major cationic form of the probe $NM7HQ^+$ (C*) can lose a proton via ESPT to generate the neutral form (K*); we utilized the unique residence behavior of the different forms of the probe to obtain insight into site-selective local solvation dynamics within the water pool of the reverse micelle. Anisotropy measurements confirmed that although C* and K* both reside in the vicinity of the AOT headgroup layer, they are separated by a few hydration layers. While C* remains tightly bound to the AOT layer, several intervening layers of water molecules are present between K* and the surfactant interface. These assignments also lend credence to the observation that while K* undergoes rapid and complete solvation within the experimental time window, the solvation of C* is extremely sluggish. Thus, although the anisotropy decay and solvation dynamics provide information corresponding to different aspects of the system, namely, the probe and the solvent environment, respectively, they provide a coherent and unified picture regarding the site-dependent mobility of our unique probe. We anticipate that the use of unique prototropic, charge-state selective probes could unravel ultrafast dynamics in confined systems by taking into account amore holistic view of the motion, diffusion, and charge transformation of the probe, and the critical interplay among these properties.

VI. References

[1] S.P. Moulik, B.K. Paul, *Adv. Colloid Interf. Sci.*, **1998**, *78*, 99–195.

[2] K. Bhattacharyya, *Acc. Chem. Res.*, **2003**, *36*, 95–101.

[3] N. Nandi, K. Bhattacharyya, B. Bagchi, *Chem. Rev.*, **2000**, *100*, 2013–2045.

[4] D.E. Moilanen, E.E. Fenn, D.B. Wong, M.D. Fayer, J. Am. Chem. Soc., **2009**, *131*, 8318–8328.

[5] H. Shirota, K. Horie, *J. Phys. Chem. B*, **1999**, *103*, 1437–1443.

[6] N.E. Levinger, L.A. Swafford, *Annu. Rev. Phys. Chem.*, **2009**, *60*, 385–406.

[7] R.K. Mitra, S.S. Sinha, S.K. Pal, *Langmuir*, **2008**, *24*, 49–56.

[8] P. Hazra, D. Chakrabarty, N. Sarkar, *Chem*. *Phys*. *Lett*., **2003**, *88*, 553–562.

[9] D.E. Moilanen, E.E. Fenn, D.B.Wong, M.D. Fayer, *J. Chem*. *Phys*., **2009**, *131*, 014704.

[10] O.-H. Kwon, D.-J. Jang, *J. Phys*. *Chem*. *B*, **2005**, *109*, 8049–8052.

[11] O.-H. Kwon, T.G. Kim, Y.-S. Lee, D.-J. Jang, *J. Phys*. *Chem*. *B*, **2006**, *110*, 11997–12004.

[12] H.-S. Tan, I.R. Piletic, M.D. Fayer, *J. Chem. Phys.*, **2005**, *122*, 174501.

[13] H. Shirota, H. Segawa, *Langmuir*, **2004**, *20*, 329–335.

[14] R.E. Riter, D.M. Willard, N.E. Levinger, *J. Phys. Chem. B*, **1998**, *102*, 2705–2714.

[15] S.-Y. Park, O.-H. Kwon, T.G. Kim, D.-J. Jang, *J. Phys. Chem. C*, **2009**, *113*, 16110–16115.

[16] M. Sedgwick, R.L. Cole, C.D. Rithner, D.C. Crans, N.E. Levinger, *J. Am. Chem. Soc.*, **2012**, *134*, 11904–11907.

[17] G. Lee, T. Jang, S. Lee, H. Oh, H. Lee, Y. Pang, *J. Mol. Liq*., **2020**, *305*, 112873.

[18] T. Jang, G. Lee, S. Lee, J. Lee, Y. Pang, *J. Mol. Liq.*, **2019**, *279*, 503–509.

[19] A. Douhal, G. Angulo, M. Gil, J.Á. Organero, M. Sanz, L.T. Tormo, *J. Phys. Chem. B*, **2007**, *111*, 5487–5493.

[20] P. Honegger, M. Schmollngruber, O. Steinhauser, *Phys. Chem. Chem. Phys.*, **2018**, *20*, 11454–11469.

[21] M. Hasegawa, T. Sugimura, Y. Suzaki, Y. Shindo, *J. Phys. Chem.*, **1994**, *98*, 2120–2124.

[22] N.A. Vodolazkaya, N.O. Mchedlov-Petrossyan, N.V. Salamanova, Y.N. Surov, A.O. Doroshenko, *J. Mol. Liq.*, **2010**, *157*, 105–112

[23] S.-Y. Park, Y.M. Lee, K. Kwac, Y. Jung, O.-H. Kwon, *Chem. Eur. J.*, **2016**, *22*, 1–6.

[24] Y.M. Lee, S.-Y. Park, H. Kim, T.G. Kim, O.-H. Kwon, *Methods Appl. Fluoresc.*, **2016**, *4*, 024004.

[25] S.-Y. Park, T.G. Kim, M.J. Ajitha, K. Kwac, Y.M. Lee, H. Kim, Y. Jung, O.-H. Kwon, *Phys. Chem. Chem. Phys.* **2016**, *18*, 24880–24889.

[26] Y.J. Kim, S. Rakshit, G.Y. Jin, P. Ghosh, Y.M. Lee, W.-W. Park, Y.S. Kim, O.-H. Kwon, *Chem. Eur. J.* **2017**, *23*, 17179–17185.

[27] D. Zhong, S.K. Pal, D. Zhang, S.I. Chan, A.H. Zewail, *Proc. Natl. Acad. Sci. U. S. A.* **2020**, *99*, 13–18.

[28] M.L. Horng, J.A. Gardecki, A. Papazyan, M. Maroncelli, *J. Phys. Chem*., **1995**, *99*, 17311–17337.

[29] D.B. Siano, D.E.Metzler, *J. Chem. Phys*., **1969**, *51*, 1856–1861.

[30] A. Kalauzi, D. Mutavdzic, D. Djikanovie, K. Radotic, M. Jeremic, *J. Fluoresc*., **2007**, *17*, 319–329.

[31] E.A. Burstein, S.M. Abornev, Y.K. Reshetnyak, *Biophys. J*., **2001**, *81*, 1699–1709.

[32] C. Adamo, D. Jacquemin, *Chem. Soc. Rev*., **2013**, *42*, 845–856.

[33] E.L. Quitevis, A.H. Marcus, M.D. Fayer, *J. Phys. Chem*., **1993**, 97*,* 5762–5769.

[34] A. Maitra, *J. Phys. Chem*., **1984**, *88*, 5122–5125.

[35] T. Kinugasa, A. Kondo, S. Nishimura, Y.Miyauchi, Y. Nishii, K.Watanabe, H. Takeuchi, *Colloids Surf. A Physicochem. Eng. Asp*., **2002**, *204*, 193–199.

[36] G. Lipari, A. Szabo, *Biophys. J*., **1980**, *30*, 489–506.

[37] G.B. Dutt, *J. Phys. Chem. B*, **2008**, *112*, 7220–7226.

[38] K. Kinosita Jr., S. Kawato, A. Ikegami, *Biophys. J*., **1997**, *20*, 289–305.

[39] J.R. Lakowicz, *Principles of Florescence Spectroscopy*, Springer, Singapore, **2010**, 331–352.

[40] B. Valeur, *Molecular Fluorescence: Principles and Applications*, Wiley, Weinheim, **2002**, 84–86.

[41] C. Lawler, M.D. Fayer, *J. Phys. Chem. B*, **2015**, *119*, 6024–6034.

[42] J. Faeder, B.M. Ladanyi, *J. Phys. Chem. B*, **2005**, *109*, 6732–6740.

[43] S. Chakraborty, S. Nandi, K. Bhattacharyya, S. Mukherjee, *ChemPhysChem*, **2019**, *20*, 3221–3227.

Acknowledgement

First of all, I would like to express my appreciation to my advisor, Professor Oh-Hoon Kwon, who is always passionate on the research. In the past few years, you have always guided me with all your heart. The many experiments, analysis skills, and methods of writing research papers that he taught me will be a great asset to not only research but my life, even if I find another career. In the future, I will always remember not only the research, but the overall attitude of life you taught me. As you blessed my future life, I also sincerely hope that all our group members including you will achieve excellent results, so that our lab will be a world-class.

In addition, I would like to express my gratefulness to my colleagues who were always smiling by my side and who have gone through the hard work of graduate school. Especially, I feel sorry rather than gratitude for Ye-Jin, who always treated me as a senior. She took on the hard work as a laboratory leader and worked harder than anyone else, but it seems that I was not very helpful for her and only made difficult things to her. However, I believe that everything she does in the future will be fine. Also, I am grateful to Won-Woo, who was the youngest but was not like the youngest. Although he was younger than me, he also gave me much of experimental help and fresh inspiration. And I am really grateful for my partner, Hak-Won who I have been with since undergraduate. At first, we really went through a lot of trial and error. I also made so lots of mistakes. But at the end of the twists and turns, we achieved our research result a certain degree. I think I always miss my graduate school life with three of you even though it was not easy. And, Professor Aniruddha, who has a hard time in other countries, it was an honor to be complete this work with you. I hope your life in Korea is full of happiness.

I would like to express my gratitude to my friends who joined the “U-Heung”, a Samul-nori club that is essential in my undergraduate school. I`ve always felt comfort in my heart from your exciting rhythms. Also, I would like to thank my "ULECA" friends who studied with me in the Department of Chemistry or Chemical and Energy Engineering. Also, thanks to "14th OT" team members who helped each other in the difficult graduate school life after entering the university.

Also, I will live with an indescribable gratitude in my heart to my respectable parents who always promised full support when I said I would go to graduate school. Thank you again to my father who always shared my difficulties and supported me silently, and to my mother who cheered me up warmly while scolded me harshly when I showed her bad habit. Thank you, Dain, my younger sister, who has hard time in Daegu. You always took care of me because you made money before me. Now, you and I are going through a really hard time in our life, but I hope that we can overcome everything and will be in a bed of roses.

Finally, I would like to thank Prof. Yung Sam Kim and Prof. Bum Suk Zhao, who were willing to accept to be a committee member of my master's thesis defense. I hope that you achieve great and prominent results in the physical chemistry fields.